PHYSICAL REVIEW RESEARCH **6**, L042049 (2024)

Letter

Quantum droplets with magnetic vortices in spinor dipolar Bose-Einstein condensates

Shaoxiong Li and Hiroki Saito [*]

Department of Engineering Science, University of Electro-Communications, Tokyo 182-8585, Japan

(Received 29 February 2024; revised 26 July 2024; accepted 23 October 2024; published 25 November 2024)

Motivated by the recent experimental realization of a Bose-Einstein condensate (BEC) of europium atoms, we investigate the self-bound droplet state for a dipolar BEC with spin degrees of freedom. Under a sufficiently weak magnetic field, the droplet has a torus shape with circulating spin vectors, which is referred to as a magnetic vortex. The ground state transforms from a torus to a cigar shape through bistability with increasing magnetic field. Dynamical change of the magnetic field causes the torus to rotate due to the Einstein–de Haas effect. The magnetic vortices form a supersolid in a confined system.

DOI: 10.1103/PhysRevResearch.6.L042049

Introduction. A magnetic flux-closure structure is a stable configuration of a ferromagnetic material in which magnetization vectors form closed loops to reduce the magnetostatic energy. This structure can be observed in a ferromagnetic material with multiple magnetic domains below the Curie temperature [1]. The magnetic flux-closure structure has also been realized within nanoscale particles [2–10], in which the magnetization vectors circulate along a toroidal loop. This state is referred to as a magnetic vortex. Nanoparticles with magnetic vortices can be used, e.g., for data storage [11], cancer therapy [12], and neuromorphic computing [13]. Such isolated objects with magnetic vortices have so far been restricted to solid materials. Is it possible to produce a liquid or gas analog of this state of matter, i.e., a self-bound droplet with a magnetic vortex? Although permanent-magnetic liquid droplets have been produced recently [14], the magnetic-vortex structure has not been observed.

Here we propose a self-bound superfluid droplet that contains a magnetic vortex. Self-bound states of Bose-Einstein condensates (BECs) have attracted much interest recently and are referred to as quantum droplets [15]. In a quantum droplet, the attractive mean-field interaction balances the repulsive beyond-mean-field effect [16], which stabilizes the system against collapse and expansion in free space. This novel state of matter was realized in a BEC with a magnetic dipole-dipole interaction (DDI) [17–21] and a Bose-Bose mixture [22–24], and various theoretical studies have been performed on these systems [25–39]. However, in experiments on quantum droplets with DDI to date, the magnetization of the system has been frozen in the direction of the strong external magnetic field. If the external magnetic field is sufficiently suppressed, spin degrees of freedom in a dipolar BEC are liberated, which allows for a spinor dipolar BEC [40–65].

In the present study, we will show that there exists a stable self-bound droplet of a spinor dipolar BEC that contains a magnetic vortex with a torus-shaped density distribution. This state is stable under a weak external magnetic field. As the magnetic field is increased, the ground state changes from the magnetic-vortex state to the well-known cigar-shaped droplet, and these two states exhibit bistability. If the external magnetic field is gradually changed, the total magnetization of the torus-shaped droplet is also changed, which induces mechanical rotation of the torus to conserve the total angular momentum, resembling the Einstein–de Haas effect. The ground state of the system confined in an elongated trap exhibits periodic alignment of the torus-shaped droplets and can be regarded as a supersolid.

For concreteness, we consider a BEC of ^{151}Eu atoms, which was recently realized experimentally [66]. A peculiar feature of ^{151}Eu is its wide range of hyperfine spins ($F = 1, \dots, 6$) with small spin-dependent contact interactions, which could be smaller than the DDI. The spin state in this system is therefore mainly determined by the DDI under a weak external magnetic field, and DDI-dominant spinor dipolar phenomena can be investigated. Although the s-wave scattering length for the $F = 6$ hyperfine state measured in Ref. [66] is too large to form a self-bound droplet, the scattering lengths for the other hyperfine spins F and those for ^{153}Eu are unknown, and formation of spinor dipolar droplets may be possible. Furthermore, the contact interactions may be controllable using microwave-induced Feshbach resonance [67]. As we will show, a spinor dipolar droplet with a magnetic vortex is possible, as long as the DDI is sufficiently larger than the spin-dependent and spin-independent contact interactions.

Formulation. We consider a BEC of ^{151}Eu atoms with hyperfine spin F at zero temperature using the beyond-mean-field approximation [25,26]. The total energy consists of six terms,

$$E = E_{\rm kin} + E_s + E_{\rm ddi} + E_{\rm LHY} + E_B + E_{\rm ext}. \tag{1}$$

The kinetic energy is given by

$$E_{\rm kin} = \frac{\hbar^2}{2M} \sum_m \int d\boldsymbol{r} |\nabla \psi_m(\boldsymbol{r})|^2, \tag{2}$$

---

[*] Contact author: hiroki.saito@uec.ac.jp

TABLE I. Magnetic moment μ, in units of the Bohr magneton μ_B, and the dipolar lengths a_{dd}, in units of the Bohr radius a_B, for ^{151}Eu with hyperfine spin F.

F	1	2	3	4	5	6
μ/μ_B	9/2	13/3	19/4	27/5	37/6	7
a_{dd}/a_B	24.72	22.92	27.54	35.60	46.42	59.82

where $\psi_m(\boldsymbol{r})$ is the macroscopic wave function for the magnetic sublevels $m = -F, -F+1, \ldots, F$, and M is the mass of an atom. The wave function is normalized as $\sum_m \int |\psi_m(\boldsymbol{r})|^2 d\boldsymbol{r} = N$, where N is the total number of atoms. The spin-independent contact interaction has the form

$$E_s = \frac{2\pi\hbar^2 a_s}{M} \int \rho^2(\boldsymbol{r}) d\boldsymbol{r}, \tag{3}$$

where a_s is the spin-independent s-wave scattering length and $\rho(\boldsymbol{r}) = \sum_m |\psi_m(\boldsymbol{r})|^2$ is the total density.

The DDI energy is given by

$$E_{\rm ddi} = \frac{\mu_0 (g\mu_B)^2}{8\pi} \int d\boldsymbol{r} d\boldsymbol{r}' \frac{\boldsymbol{f}(\boldsymbol{r}) \cdot \boldsymbol{f}(\boldsymbol{r}') - 3[\boldsymbol{f}(\boldsymbol{r}) \cdot \boldsymbol{e}][\boldsymbol{f}(\boldsymbol{r}') \cdot \boldsymbol{e}]}{|\boldsymbol{r} - \boldsymbol{r}'|^3}, \tag{4}$$

where μ_0 is the magnetic permeability of the vacuum, g is the hyperfine g factor, μ_B is the Bohr magneton, $\boldsymbol{f}(\boldsymbol{r}) = \sum_{mm'} \psi_m^*(\boldsymbol{r}) (\boldsymbol{S})_{mm'} \psi_{m'}(\boldsymbol{r})$ with $\boldsymbol{S}$ being the spin matrix, and $\boldsymbol{e} = (\boldsymbol{r} - \boldsymbol{r}')/|\boldsymbol{r} - \boldsymbol{r}'|$. The relative strength of the DDI is characterized by $\varepsilon_{\rm dd} = a_{\rm dd}/a_s$, where $a_{\rm dd} = \mu_0 \mu^2 M/(12\pi\hbar^2)$ is the dipolar length. The magnetic moment of an atom with hyperfine spin F, total electron spin S, and nuclear spin I with orbital angular momentum $L = 0$ is given by $\mu = g\mu_B F$, with the g factor [68]

$$g = \frac{F(F+1) + S(S+1) - I(I+1)}{F(F+1)}. \tag{5}$$

For the electronic ground state of ^{151}Eu (and also ^{153}Eu), $S = 7/2$ and $I = 5/2$. The magnetic moment μ and the dipolar length $a_{\rm dd} = \mu_0 \mu^2 M/(12\pi\hbar^2)$ of ^{151}Eu are given in Table I. The spin distribution is mainly determined by the DDI if $a_{\rm dd}$ is sufficiently larger than the spin-dependent scattering lengths that consist of the differences Δa among the scattering lengths $a_{0,2,\ldots,2F}$ in collisional spin channels. The values of Δa are predicted to be relatively small for europium atoms [66,69,70] and we ignore the spin-dependent contact interaction. The effects of the spin-dependent contact interactions will be discussed later.

As will be confirmed numerically, the spin state is almost fully polarized in the droplet. In this case, we do not need to consider the Lee-Huang-Yang (LHY) corrections for spinor BECs, and we use the LHY correction for a fully polarized dipolar BEC, which has the same form as that of the single-component dipolar BEC [71,72]. Under the local density approximation, the LHY correction is written as [25,26,73–75]

$$E_{\rm LHY} = \frac{2}{5} \frac{32}{3\sqrt{\pi}} \frac{4\pi\hbar^2}{M} a_s^{5/2} \chi(\varepsilon_{\rm dd}) \int \rho^{5/2}(\boldsymbol{r}) d\boldsymbol{r}, \tag{6}$$

where $\chi(\varepsilon_{\rm dd})$ is the real part of $\int_0^\pi d\theta \sin\theta [1 + \varepsilon_{\rm dd}(3\cos^2\theta - 1)]^{5/2}/2$.

In the presence of an external magnetic field $\boldsymbol{B}(\boldsymbol{r})$, the linear Zeeman energy has the form $E_B = g\mu_B \int \boldsymbol{f}(\boldsymbol{r}) \cdot \boldsymbol{B}(\boldsymbol{r}) d\boldsymbol{r}$. The ratio of the quadratic Zeeman energy to the linear Zeeman energy is estimated to be $\mu B/\Delta_{\rm hf} \sim 10^{-4}$ at most for the present magnetic field, ~0.1 mG, and the quadratic Zeeman energy can be neglected even for the relatively small hyperfine splitting $\Delta_{\rm hf}/\hbar \sim 100$ MHz for a europium atom [77]. The external potential energy is given by $E_{\rm ext} = \int \rho(\boldsymbol{r}) V_{\rm ext}(\boldsymbol{r}) d\boldsymbol{r}$; no external potential is applied ($V_{\rm ext} = 0$) in "Results" sections except "Supersolid in trapped systems" section.

The Gross-Pitaevskii (GP) equation is obtained as $i\hbar \partial\psi_m/\partial t = \delta E/\delta\psi_m^*$. The explicit form is given by

$$\begin{aligned} i\hbar \frac{\partial\psi_m}{\partial t} &= -\frac{\hbar^2}{2M}\nabla^2\psi_m + V_{\rm ext}\psi_m + \frac{4\pi\hbar^2 a_s}{M}\rho\psi_m \\ &\quad + \frac{32}{3\sqrt{\pi}} \frac{4\pi\hbar^2 a_s^{5/2}}{M} \chi(\varepsilon_{\rm dd}) \rho^{3/2} \psi_m \\ &\quad + g\mu_B (\boldsymbol{B} + \boldsymbol{B}_{\rm dd}) \cdot \sum_{m'} (\boldsymbol{S})_{mm'} \psi_{m'}, \end{aligned} \tag{7}$$

where the magnetic field $\boldsymbol{B}_{\rm dd}$ produced by the dipole-dipole interaction (DDI) is defined as

$$\boldsymbol{B}_{\rm dd}(\boldsymbol{r}) = \frac{g\mu_B\mu_0}{4\pi} \int d\boldsymbol{r}' \frac{\boldsymbol{f}(\boldsymbol{r}') - 3[\boldsymbol{f}(\boldsymbol{r}') \cdot \boldsymbol{e}]\boldsymbol{e}}{|\boldsymbol{r} - \boldsymbol{r}'|^3}. \tag{8}$$

To obtain the ground state or metastable state, the GP equation is propagated in imaginary time, in which i on the left-hand side of the GP equation is replaced with -1. The GP equation is numerically solved using the pseudospectral method with typical spatial and time steps $dx \sim 0.01$ μm and $dt \sim 0.1$ μs.

Results: Torus-shaped droplets. First, we consider the case in which the external magnetic field B is zero. Figure 1 shows a typical ground state, which has a torus shape, in contrast to the usual cigar-shaped droplet in a strong magnetic field [17–21]. The magnetization vectors $\boldsymbol{f}$ circulate along the torus, as shown by the arrows in Fig. 1(a), which is a magnetic vortex. The magnetic-vortex state with a torus shape is an energetically favorable state because all the spin vectors are aligned in a head-to-tail manner, which reduces the DDI energy. This is also understood from the fact that the flux-closure structure is stable in magnetic materials. This is an example of a self-bound droplet of a fluid containing a magnetic vortex; in previous studies, magnetic-vortex states have been proposed only for trapped systems [45,47].

In the LHY energy in Eq. (6), we assumed that the spin state is fully polarized, and here we examine the validity of this assumption. Figure 1(c) shows the distributions of the atomic density ρ and magnetization density $|\boldsymbol{f}|$, which indicate that the spin is almost fully polarized, i.e., $|\boldsymbol{f}|/\rho \simeq F = 1$, except near the center. This result justifies the use of Eq. (6) since the LHY correction is important only in the high-density region to counteract the collapse. The central hole of the torus is mainly occupied by the $m = 0$ component since the $m \neq 0$ components have topological defects at the center, as shown in Fig. 1(b).

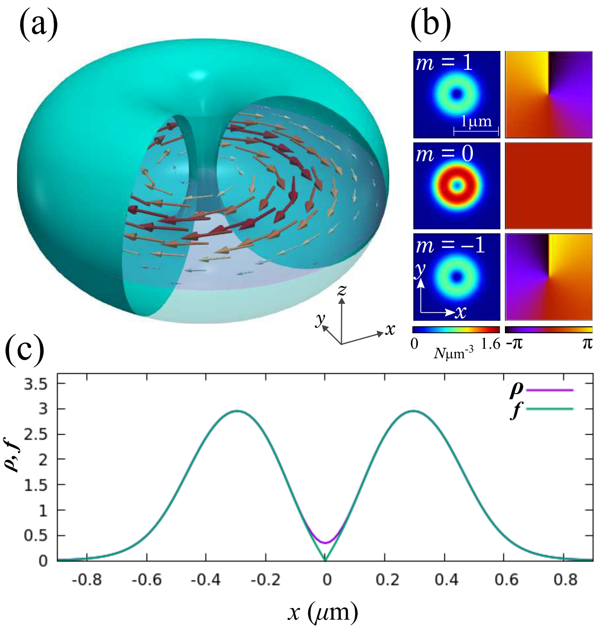

FIG. 1. Self-bound ground state with magnetic vortex for $F = 1$, $N = 15\,000$, $\varepsilon_{\rm dd} = 1.2$, and $B = 0$. The origin and z axis are taken as the center and symmetry axis of the torus, respectively. (a) Isodensity surface at half of maximum density. The arrows represent the magnetization $\boldsymbol{f}$ on the $z = 0$ plane. (b) Density and phase distributions of components $m = 1$, 0, and -1 on the $z = 0$ plane. (c) Distributions of ρ and $|\boldsymbol{f}|$ along the x axis.

We study the stability of the torus-shaped droplet against external disturbances. First, we prepare the torus-shaped droplet state in the presence of a random potential by the imaginary-time evolution of the GP equation. The random potential is produced by placing random numbers on a numerical grid and low-pass-filtering them using a cutoff wave number of $2\pi/(0.25\ \mu\text{m})$. The initial disturbed droplet is shown in Fig. 2(a) ($t = 0$ ms). At $t = 0$, the random potential is removed and the real-time evolution is started, as shown in Fig. 2. First, a small number of atoms are emitted from the droplet, as shown in Fig. 2(b) ($t = 0.15$ ms), since the Bogoliubov modes with energies larger than $|\mu|$ are unbound [30], where $\mu < 0$ is the chemical potential of the droplet state. After that, an axial stretching mode remains (see the movie in the Supplemental Material [76]), which has a period of $\simeq 1.6$ ms. The energy of this mode is smaller than $|\mu| \simeq 2\pi\hbar/(0.8\ \text{ms})$ and the mode is thus bound to the droplet. In the numerical simulation, emitted atoms that travel far from the droplet are removed, so that they do not affect the droplet again. We have numerically confirmed that the system exhibits behavior similar to Fig. 2 for different N, $\varepsilon_{\rm dd}$, and F. Thus, the torus-shaped droplet with a magnetic vortex is rather robust against external disturbances.

Figure 3 shows the parameter dependence of the density profile. The size of the droplet increases with the number of atoms, N, while the size of the central hole appears almost unchanged [left and middle panels of Fig. 3(a)]. For a larger spin $F = 6$, on the other hand, the hole of the torus is significantly enlarged [right panel of Fig. 3(a)]. As shown in Eq. (11), this is due to the kinetic energy that arises from the spin winding, which is proportional to F.

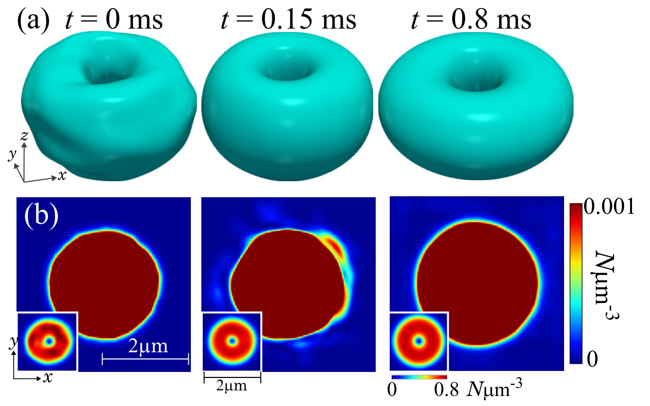

FIG. 2. Dynamics of torus-shaped droplet with $F = 1$, $N = 80\,000$, $\varepsilon_{\rm dd} = 1.2$, and $B = 0$. The initial state is the ground state with a random potential. (a) Isodensity surface at half of maximum density. A movie showing the dynamics is provided in the Supplemental Material [76]. (b) Density profiles on the $z = 0$ plane. Note that the color ranges in the main panels and insets are different. The density hole at the center of the torus cannot be seen for the narrow color range in the main panels.

Variational analysis. To analyze the parameter dependence of the torus-shaped droplet, we perform the variational analysis. We employ the variational wave function as

$$\boldsymbol{\Psi}_v(\boldsymbol{r}) = \sqrt{\rho_v(r, z)}\, e^{-iS_z\phi} \boldsymbol{\zeta}^{(y)}, \tag{9}$$

where (r, ϕ, z) are the cylindrical coordinates, and $\boldsymbol{\zeta}^{(y)}$ represents the spin state fully polarized in the y direction with $\sum_m |\zeta_m^{(y)}|^2 = 1$. The z axis is taken as the symmetry axis of

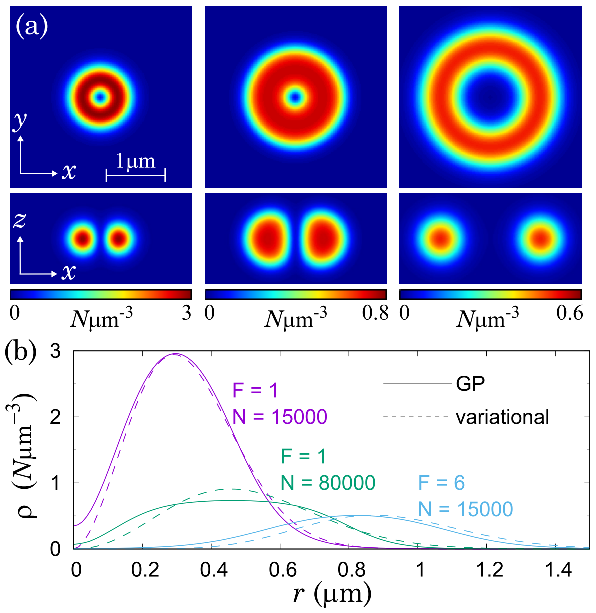

FIG. 3. Self-bound ground states for $(F, N, \varepsilon_{\rm dd}) = (1, 15\,000, 1.2)$, $(1, 80\,000, 1.2)$, and $(6, 15\,000, 1.3)$. (a) Density distributions obtained by GP equation. Cross sections on two symmetric planes are shown. (b) Density distributions $\rho(r, z = 0)$ obtained by GP equation (solid lines) and variational method (dashed lines).

the torus. The matrix $e^{-iS_z\phi}$ rotates the spin vector to make a magnetic vortex. We propose a torus-shaped variational density as

$$\rho_v(r,z) = \frac{N}{\pi^{3/2}\sigma_r^{2\lambda+2}\sigma_z\Gamma(\lambda+1)} r^\lambda e^{-\frac{r^2}{\sigma_r^2}-\frac{z^2}{\sigma_z^2}}, \tag{10}$$

where $\sigma_r > 0$, $\sigma_z > 0$, and $\lambda > 0$ are variational parameters and Γ is the gamma function. Substituting Eqs. (9) and (10) into the kinetic energy $E_{\rm kin}$, we obtain

$$\begin{aligned} E_{\rm kin} &= \frac{\hbar^2}{2M}\int d\boldsymbol{r}\left[(\nabla\sqrt{\rho_v})^2 + \frac{F}{2r^2}\rho_v\right] \\ &= \frac{N\hbar^2}{2M}\left[\frac{1}{2\sigma_r^2}\left(2+\frac{F}{\lambda}\right) + \frac{1}{2\sigma_z^2}\right], \end{aligned} \tag{11}$$

where the term proportional to F arises from the winding of the spin vector. The central hole of the torus increases with F due to this term, as shown in Fig. 3. For the present form of the variational wave function, the z component of the magnetization $f_z(\boldsymbol{r})$ vanishes and the integral part I of the DDI energy $E_{\rm ddi}$ can be expressed as

$$\begin{aligned} I &= \int \frac{d\boldsymbol{r}d\boldsymbol{r}'}{|\boldsymbol{r}-\boldsymbol{r}'|^3}\{\boldsymbol{f}(\boldsymbol{r})\cdot\boldsymbol{f}(\boldsymbol{r}') - 3[\boldsymbol{f}(\boldsymbol{r})\cdot\boldsymbol{e}][\boldsymbol{f}(\boldsymbol{r}')\cdot\boldsymbol{e}]\} \\ &= \int \frac{d\boldsymbol{r}d\boldsymbol{r}'}{|\boldsymbol{r}-\boldsymbol{r}'|^3}\bigg\{-\frac{1}{2}f_+(\boldsymbol{r})f_-(\boldsymbol{r}')(1-3e_z^2) \\ &\quad - \frac{3}{4}[f_+(\boldsymbol{r})f_+(\boldsymbol{r}')e_-^2 + f_-(\boldsymbol{r})f_-(\boldsymbol{r}')e_+^2]\bigg\} \\ &= \int \frac{d\boldsymbol{k}}{(2\pi)^3}\bigg\{\frac{2\pi}{3}(1-3\cos^2\alpha)\tilde{f}_+(-\boldsymbol{k})\tilde{f}_-(\boldsymbol{k}) \\ &\quad + \pi\sin^2\alpha[e^{-2i\beta}\tilde{f}_+(-\boldsymbol{k})\tilde{f}_+(\boldsymbol{k}) + e^{2i\beta}\tilde{f}_-(-\boldsymbol{k})\tilde{f}_-(\boldsymbol{k})]\bigg\}, \end{aligned} \tag{12}$$

where α and β are the polar and azimuthal angles in the $\boldsymbol{k}$ space, respectively, $\tilde{f}_\pm(\boldsymbol{k})$ is the Fourier transform of $f_\pm(\boldsymbol{r}) = f_x(\boldsymbol{r}) \pm i f_y(\boldsymbol{r})$, and the convolution theorem was used in the third equality. Noting that $\tilde{f}_\pm(\boldsymbol{k})$ is proportional to $\pm e^{\pm i\beta}$ and $\tilde{f}_\pm(-\boldsymbol{k}) = -\tilde{f}_\pm(\boldsymbol{k})$ for the forms of Eqs. (9) and (10), Eq. (12) can be reduced to

$$\begin{aligned} I &= -\frac{4\pi}{3}\int\frac{d\boldsymbol{k}}{(2\pi)^3}|\tilde{f}_+(\boldsymbol{k})|^2 \\ &= -\frac{4\pi F^2}{3}\int d\boldsymbol{r}\rho_v^2(\boldsymbol{r}), \end{aligned} \tag{13}$$

which gives

$$E_{\rm ddi} = -\frac{2\pi\hbar^2 a_{\rm dd}}{M}\int d\boldsymbol{r}\rho_v^2(\boldsymbol{r}). \tag{14}$$

This result indicates that $E_{\rm ddi}/E_s = -\varepsilon_{\rm dd}$, and therefore $\varepsilon_{\rm dd} > 1$ is the necessary condition for the droplet to be bound by the attractive part of the DDI. Using Eq. (10), the DDI and s-wave interaction energies are calculated to be

$$\frac{ME_{\rm ddi}}{N\hbar^2} = -\varepsilon_{\rm dd}\frac{ME_s}{N\hbar^2} = -\frac{Na_{\rm dd}\Gamma(\lambda+1/2)}{\sqrt{2}\pi\Gamma(\lambda+1)\sigma_r^2\sigma_z}. \tag{15}$$

The LHY energy in Eq. (6) is obtained as

$$\frac{ME_{\rm LHY}}{N\hbar^2} = \frac{2^{(5\lambda+17)/2}N^{3/2}a^{5/2}\lambda\Gamma(5\lambda/2)\chi(\varepsilon_{\rm dd})}{3\pi^{7/4}5^{(5\lambda+3)/2}\Gamma^{5/2}(\lambda+1)\sigma_r^3\sigma_z^{3/2}}. \tag{16}$$

The total variational energy is given by the sum of these energies.

We minimize the variational energy with respect to the variational parameters σ_r, σ_z, and λ, which is numerically performed using the Newton-Raphson method. Figure 3(b) compares the density distributions $\rho(r, z=0)$ obtained by the GP equation and by the variational method. The two distributions agree well with each other. For $N = 80\,000$, the deviation near the peak becomes significant since the flat-top tendency of the density distribution is not taken into account in Eq. (10). The density at $r = 0$ must vanish for the fully polarized assumption in Eq. (9), whereas the center is slightly occupied for the GP results.

Using the variational method, we can estimate the critical number of atoms below which the minimum or local minimum of the variational energy disappears, namely, the stationary state does not exist and the system always expands. Figure 4(a) shows the critical number of atoms, where the lines are obtained by the variational method and the plots by the GP equation. The variational method can predict the critical number of atoms very well, which facilitates the study of this system because the numerical cost for the GP simulation is much higher than that for the variational method, especially near the critical stability line where convergence of the imaginary-time evolution is slow.

Figures 4(b)–4(e) show the variational parameters that minimize the variational energy. The droplet size σ_r (also σ_z) decreases with $\varepsilon_{\rm dd}$ due to the attractive nature of the DDI, as shown in Fig. 4(b), while σ_r increases with N except near the critical number of atoms, as shown in Fig. 4(c). In Figs. 4(b) and 4(c), the droplet size steeply increases near the critical values (left-hand edges of the lines) since the droplet is about to become unbound. Figure 4(d) shows the aspect ratio $A(\lambda)$ for the torus defined by

$$A(\lambda) = \frac{\langle r\rangle}{\sqrt{\langle r^2\rangle - \langle r\rangle^2}} = \left[\frac{(\lambda+1)\Gamma^2(\lambda+1)}{\Gamma^2(\lambda+3/2)} - 1\right]^{-1/2}, \tag{17}$$

where $\langle\cdot\rangle$ represents the expectation value with respect to the variational wave function. The aspect ratio $A(\lambda)$ in Eq. (17) is a monotonically increasing function of λ. We find from Figs. 4(d) and 4(e) that $A(\lambda)$ is largely dependent on the spin F. This is due to the term proportional to F/λ in Eq. (11), i.e., the kinetic energy arising from the spin winding. The aspect ratio is not significantly sensitive to $\varepsilon_{\rm dd}$ or N, as shown in Figs. 4(d) and 4(e).

To clarify the physical mechanism for the formation of the torus-shaped droplet, we consider the well-known cigar-shaped droplet for comparison. We assume that the spin is fully polarized in the z direction and employ the Gaussian variational wave function as

$$\psi_{m=F}(\boldsymbol{r}) = \frac{N^{1/2}}{\pi^{3/4}d_r d_z^{1/2}} e^{-\frac{x^2+y^2}{2d_r^2}-\frac{z^2}{2d_z^2}} \tag{18}$$

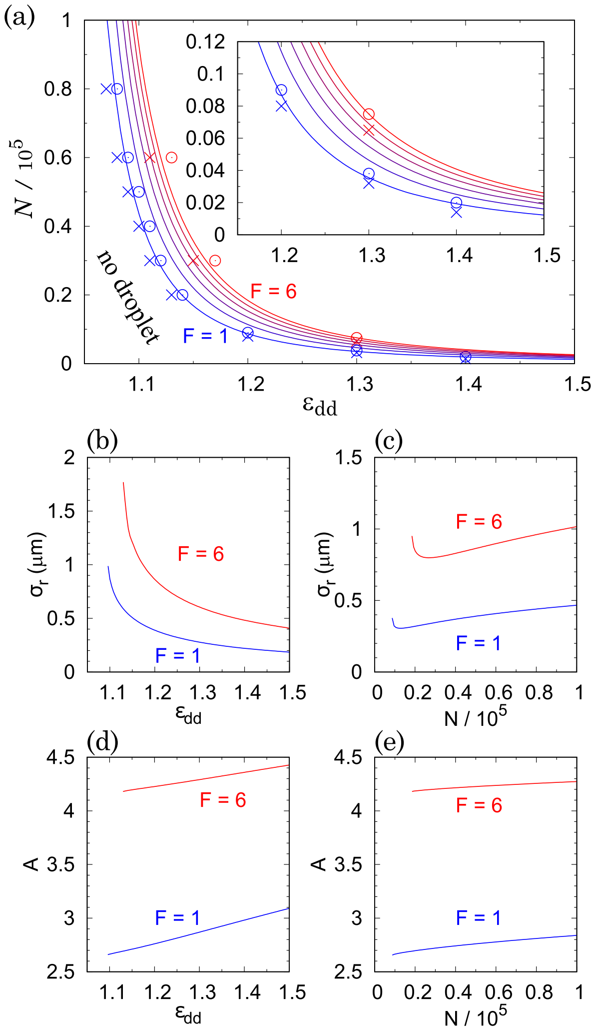

FIG. 4. (a) Lines: Critical number of atoms above which the torus-shaped droplet is stable, obtained by the variational method. Below the lines, the atomic cloud always expands. The six lines represent $F = 1, \ldots, 6$, from left to right. The circles (crosses) indicate that the stable torus-shaped droplet exists (does not exist) for $F = 1$ (blue) and $F = 6$ (red), obtained by the GP equation. Inset: A magnification of the main panel. (b)–(e) $\varepsilon_{\rm dd}$ and N dependence of variational parameters that minimize variational energy. (b) Dependence of σ_r on $\varepsilon_{\rm dd}$, (c) σ_r on N, (d) A on $\varepsilon_{\rm dd}$, and (e) A on N for $F = 1$ and 6. $N = 50\,000$ in (b) and (d), and $\varepsilon_{\rm dd} = 1.2$ in (c) and (e).

and $\psi_{m<F}(\boldsymbol{r}) = 0$, where d_r and d_z are the variational parameters. Substituting Eq. (18) into the s-wave interaction energy E_s and the DDI energy $E_{\rm ddi}$, we obtain

$$\frac{E_{\rm ddi}}{E_s} = -\varepsilon_{\rm dd} f(d_r/d_z), \tag{19}$$

where

$$f(\kappa) = \frac{1}{1-\kappa^2}\left(2\kappa^2 + 1 - \frac{3\kappa^2}{\sqrt{1-\kappa^2}} \tanh^{-1}\sqrt{1-\kappa^2}\right). \tag{20}$$

The function $f(\kappa)$ is a monotonically decreasing function with $f(0) = 1$. This indicates that a very elongated cigar shape with $d_r \ll d_z$ minimizes the DDI energy; however, a small d_r leads to a kinetic energy cost. Thus, the DDI energy of the torus-shaped droplet in Eq. (15) that satisfies $E_{\rm ddi}/E_s = -\varepsilon_{\rm dd}$ is optimal, which cannot be achieved by the cigar-shaped droplet. The large negative DDI energy of the torus-shaped droplet is due to the flux-closure structure of the magnetization. This is why the torus-shaped droplet is energetically favorable compared with the cigar-shaped droplet for zero magnetic field.

Effect of spin-dependent interaction. We investigate the effect of the spin-dependent interaction, which is neglected above. Since the spin state is almost fully polarized in the torus-shaped droplet, as shown in Fig. 1(c), the most relevant term in the spin-dependent interaction energy is the $\boldsymbol{f}\cdot\boldsymbol{f}$ term given by

$$E_f = \frac{2\pi\hbar^2 a_f}{MF^2}\int \boldsymbol{f}(\boldsymbol{r})\cdot\boldsymbol{f}(\boldsymbol{r})d\boldsymbol{r}, \tag{21}$$

where $a_f = a_{2F} - a_s$ with a_{2F} being the scattering length for a colliding channel with a total spin $2F$, and a_s being the spin-independent scattering length. Assuming that the spin state is fully polarized everywhere, the sum of the spin-independent interaction energy E_s and E_f has the form

$$\begin{aligned} E_s + E_f &\simeq \frac{2\pi\hbar^2(a_s + a_f)}{M}\int \rho^2(\boldsymbol{r})d\boldsymbol{r} \\ &= \frac{2\pi\hbar^2 a_{2F}}{M}\int \rho^2(\boldsymbol{r})d\boldsymbol{r}. \end{aligned} \tag{22}$$

The other spin-dependent energies vanish for the fully polarized spin state. Thus, the effective ratio between the DDI and contact interaction energies is found to be

$$\varepsilon_{\rm dd}^{\rm eff} = \frac{a_{\rm dd}}{a_s + a_f} = \frac{a_{\rm dd}}{a_{2F}}. \tag{23}$$

To confirm Eq. (23), we study the stability of the torus-shaped droplet by numerically solving the GP equation for $F = 1$, where the terms

$$\frac{\delta E_f}{\delta\psi_m^*(\boldsymbol{r})} = \frac{4\pi\hbar^2 a_f}{M}\boldsymbol{f}(\boldsymbol{r})\cdot\sum_{m'}(\boldsymbol{S})_{mm'}\psi_{m'}(\boldsymbol{r}) \tag{24}$$

are added to the right-hand side and a_s in the LHY correction term is replaced with $a_s + a_f$ [71]. Figure 5 shows the stability diagram with respect to a_s and a_f. We find that the stability boundary follows $a_s + a_f \simeq$ constant, which confirms that the stability of the droplet is determined by $\varepsilon_{\rm dd}^{\rm eff}$ in Eq. (23).

If a_f is positive and larger than $a_{\rm dd}$, the ferromagnetic spin state no longer minimizes the energy and the polar state becomes energetically favorable (for $F = 1$). In this case, the self-bound state is not formed, even if $\varepsilon_{\rm dd}^{\rm eff} \gtrsim 1$ is satisfied (with negative a_s). For the parameters in Fig. 5, we have numerically confirmed that the torus-shaped droplet exists only for $a_f/a_{\rm dd} \lesssim 0.9$. In the presence of spin-dependent energies other than Eq. (21) (for $F > 1$), the stability condition for the torus-shaped droplet will be similar, i.e., $|a_{\rm sd}| \lesssim a_{\rm dd}$, where $a_{\rm sd}$ is the corresponding spin-dependent scattering length. This condition can also be expressed as $|\Delta a| \lesssim a_{\rm dd}$ since the spin-dependent scattering lengths $a_{\rm sd}$ are linear combinations of differences Δa among the scattering lengths for colliding spin channels $a_{0,2,\ldots,2F}$. To summarize, the stability condition

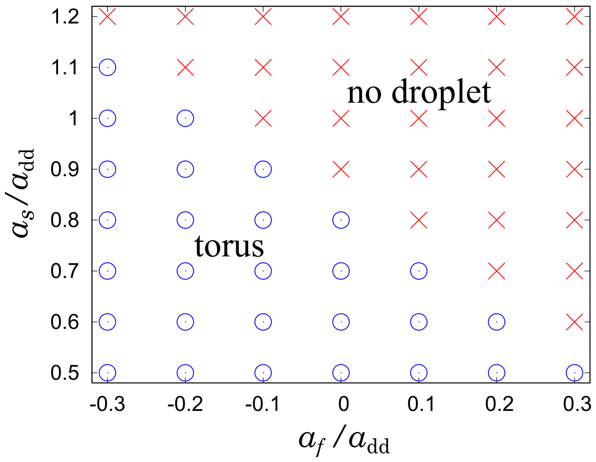

FIG. 5. Stability diagram for the torus-shaped droplet obtained by imaginary-time evolution of the GP equation including the spin-dependent interaction term in Eq. (24), where $F = 1$, $N = 15\,000$, and $B = 0$.

of the torus-shaped droplet is $a_{2F} \lesssim a_{\rm dd}$ and $|\Delta a| \lesssim a_{\rm dd}$ in the presence of the spin-dependent interactions.

Effect of external magnetic field. We examine the effect of the external magnetic field applied in the z direction. Figure 6(a) shows a typical ground state for a large magnetic field B_z, where the droplet has a cigar shape, as observed experimentally. The spin is almost polarized in the z direction, whereas it is slightly tilted around both edges of the cigar shape and exhibits a flowerlike structure [45]. Figure 6(b) shows the stability diagram with respect to N and B_z. There is a critical magnetic field, above which the torus-shaped droplet becomes unstable, whereas the cigar-shaped droplet becomes unstable below some critical magnetic field. In Fig. 6(b), there is a bistability region in which both torus-shaped and cigar-shaped droplets are stationary (both circles and squares are marked).

Figure 6(c) reveals the bistability with plots of the energy E and the averaged magnetization in the z direction $F_z = \int f_z d\boldsymbol{r}/N$ for both droplets. The bistability ranges from $B_z \simeq 0.03$ to $\simeq 0.17$ mG, and the energies of the two droplets cross at $B_z \simeq 0.14$ mG. The direction of the torus-shaped droplet is fixed by the magnetic field in such a way that the toroidal plane is parallel to the z direction, as shown in the inset of Fig. 6(c). In this inset, the right-hand side of the torus becomes slightly thicker than the left-hand side, which results in an increase in F_z.

The increase in magnetization F_z with magnetic field B_z implies the emergence of the Einstein–de Haas effect [78,79]; if B_z is increased adiabatically, the spin angular momentum F_z will increase, which must be accompanied by a decrease in the orbital angular momentum $L_z = -i \int \sum_m d\boldsymbol{r} \psi_m^* (x\partial_y - y\partial_x)\psi_m^*$ (in unit of $\hbar$) to conserve the total angular momentum. Figure 7 demonstrates the dynamics of the Einstein–de Haas effect, where the initial droplet state is prepared for $\boldsymbol{B} = 0$ with the symmetry axis in the y direction, and B_z is linearly increased in the first 10 ms. As expected, the droplet begins to rotate around the z axis, where the total angular momentum $F_z + L_z$ is maintained to be zero. We note that such mechanical rotation of the torus is a clearer manifestation of the Einstein–de Haas effect than that in a trapped system [41,42].

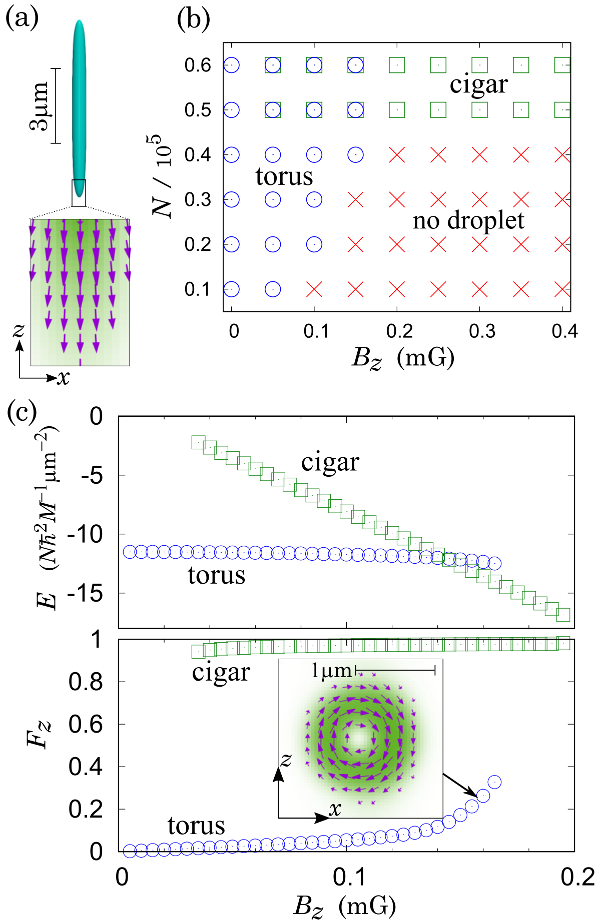

FIG. 6. Effects of magnetic field B_z obtained by the GP equation for $F = 1$ and $\varepsilon_{\rm dd} = 1.2$. (a) Isodensity surface at half of maximum density of the ground state for $N = 50\,000$ and $B_z = 0.2$ mG. The panel shows a magnification of the magnetization on the symmetry ($y = 0$) plane. (b) Stability diagram. The regions marked by circles and squares, respectively, indicate that the torus-shaped and cigar-shaped droplets are stable or metastable. In the region marked by crosses, the system is unstable against expansion. (c) B_z dependence of energy E and averaged magnetization F_z of torus-shaped and cigar-shaped droplets with $N = 50\,000$. Inset: ρ and $\boldsymbol{f}$ distributions for the torus-shaped droplet for $B_z = 0.16$ mG, where the cross section is taken for the symmetry ($y = 0$) plane.

Supersolid in trapped systems. We consider the ground state of the system confined in an elongated harmonic potential,

$$V_{\rm ext}(\boldsymbol{r}) = \frac{M}{2}\left(\omega_x^2 x^2 + \omega_y^2 y^2 + \omega_z^2 z^2\right), \tag{25}$$

with $(\omega_x, \omega_y, \omega_z) = 2\pi \times (100, 3000, 3000)$ Hz. Figure 8 shows the density and spin distributions for the ground state, in which multiple droplets with magnetic vortices are aligned along the x axis with alternate circulations of the magnetic vortices. This state can be regarded as a one-dimensional supersolid because the ground state has a (quasi)periodicity that breaks the (quasi)translation symmetry (in the x direction); each droplet is connected to adjacent droplets, which enables

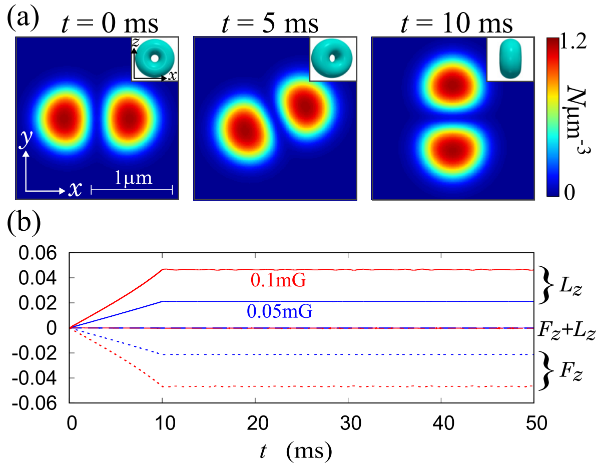

FIG. 7. Einstein–de Haas effect in torus-shaped droplet for $F = 1$, $\varepsilon_{\text{dd}} = 1.2$, and $N = 50\,000$. The initial state is the ground state for $\boldsymbol{B} = 0$ with its symmetry axis in the y direction. (a) Time evolution of density distribution on the $z = 0$ plane (main panels) and isodensity surface observed from the $-y$ direction (insets), where the magnetic field is linearly ramped up from $B_z = 0$ to 0.1 mG in the first 10 ms. See the Supplemental Material [76] for a movie of the dynamics. (b) Time evolution of orbital angular momentum L_z (solid lines), spin angular momentum F_z (dotted lines), and total angular momentum $F_z + L_z$ (dashed lines) for $B_z = 0.05$ mG [blue (dark gray)] and 0.1 mG [red (light gray)].

superflow between them. We note that the dipolar supersolid of cigar-shaped droplets [80–82] also requires confinement in one or two directions, i.e., restricted geometry is required for the dipolar BEC to split into multiple droplets. If the trap in the y or z direction in Fig. 8 is removed, the ground state becomes a large single droplet with a magnetic vortex.

The phase coherence between the droplets is necessary for the supersolidity. In general, the $F = 1$ ferromagnetic spin state can be expressed as [83]

$$e^{i(\theta-\gamma)}\begin{pmatrix} e^{-i\alpha}\cos^2\frac{\beta}{2} \\ \sqrt{2}\cos\frac{\beta}{2}\sin\frac{\beta}{2} \\ e^{i\alpha}\sin^2\frac{\beta}{2} \end{pmatrix}, \tag{26}$$

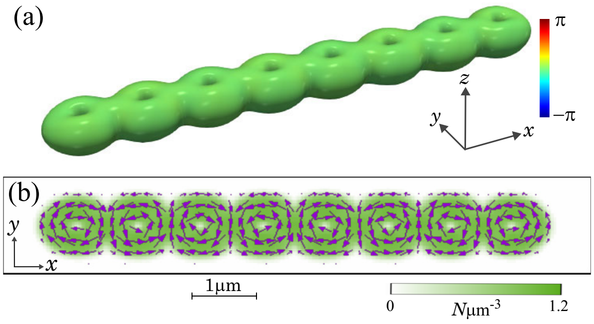

FIG. 8. Ground state for $F = 1$, $N = 4 \times 10^5$, $\varepsilon_{\text{dd}} = 1.5$, and $B_z = 0$ in cigar-shaped harmonic potential given in Eq. (25). (a) Isodensity surface at half of maximum density. The color on the surface represents the overall phase. (b) Distributions of density ρ and magnetization $\boldsymbol{f}$ on $z = 0$ plane.

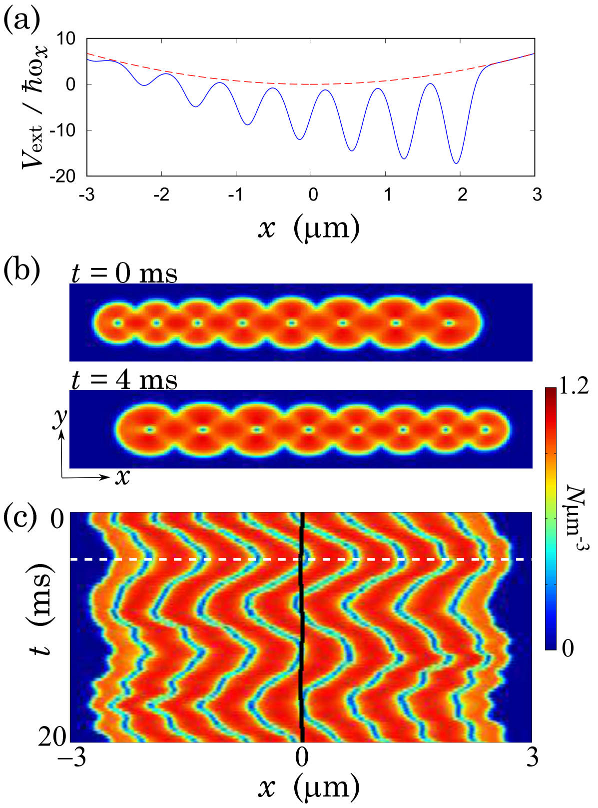

FIG. 9. Out-of-phase Goldstone mode for torus-shaped droplets in cigar-shaped harmonic potential. The parameters are the same as those in Fig. 8. (a) Additional potential V_{add} in Eq. (27) used to prepare the initial state. The solid line plots the harmonic potential plus V_{add}, and the dashed line plots the harmonic potential. (b) Snapshots of density distribution on the $z = 0$ plane at $t = 0$ and 4 ms. The size of the panels is 6×1 μm. (c) Time evolution of one-dimensional density distribution $\rho(x, y = 0, z = 0, t)$, where V_{add} is removed at $t = 0$. The black line represents the center-of-mass position $\langle x \rangle$ at each time. The white dashed line indicates $t = 4$ ms. A movie showing the dynamics is provided in the Supplemental Material [76].

where $e^{i\theta}(1, 0, 0)$ is rotated by the Euler angles α, β, and γ. The overall phase $\theta - \gamma$ is therefore obtained by $\arg[\psi_0(\boldsymbol{r})]$ or $\arg[\psi_1(\boldsymbol{r})\psi_{-1}(\boldsymbol{r})]/2$. The color in Fig. 8(a) represents the overall phase of the droplets, which is uniform everywhere in the system, showing the phase coherence between the droplets. We have numerically confirmed that the phase coherence is robust against noise. To further clarify the supersolidity, we excite the out-of-phase Goldstone mode [84]. In addition to the cigar-shaped harmonic potential, we impose a potential V_{add} as

$$V_{\text{add}}(\boldsymbol{r}) = -V_0 \sum_{\ell=0}^{7} (2\ell + 1) e^{-[(x+x_0-x_1\ell)/\sigma]^2}, \tag{27}$$

in the preparation of the initial state, where we take $V_0 = 1.3\hbar\omega_x$, $x_0 = 2.95$ μm, $x_1 = 0.7$ μm, and $\sigma = 0.2$ μm. This additional potential and the ground-state density distribution are shown in Figs. 9(a) and 9(b), respectively. Due to the potential V_{add}, the droplets have an imbalanced distribution; droplets on the right-hand side are enlarged, while those on the left-hand side are shrunk. At $t = 0$, the potential V_{add} is removed and the subsequent dynamics is shown in Fig. 9(c). One can clearly see that the pattern oscillates in the x direction with a period of $\simeq$8 ms. The center-of-mass position,

$$\langle x\rangle = \frac{1}{N}\int d\boldsymbol{r} x\rho(\boldsymbol{r}), \tag{28}$$

is shown as the black line in Fig. 9(c), which is almost at rest. This counterintuitive dynamics in which the pattern largely moves while the center-of-mass position remains unchanged is the manifestation of the out-of-phase Goldstone mode [84], which is a hallmark of supersolidity, namely, the superflow compensates for the movement of the pattern to maintain the center-of-mass position.

Conclusions and discussion. To summarize, we have investigated a self-bound droplet in a spinor dipolar BEC. For a large number of atoms, large $\varepsilon_{\rm dd}$, and a small magnetic field, there exists a stable self-bound torus-shaped droplet that contains a magnetic vortex (Fig. 1), which is stable against disturbances (Fig. 2). We proposed a variational wave function for the torus-shaped droplet, which agreed well with the GP results (Figs. 3 and 4). The torus-shaped droplet is stable even in the presence of the spin-independent interactions, if the dipolar length $a_{\rm dd}$ is sufficiently larger than the relevant scattering lengths (Fig. 5). For some range of the magnetic field, the system exhibits bistability between the torus- and cigar-shaped droplets (Fig. 6). The torus-shaped droplet exhibits the Einstein–de Haas effect as the applied magnetic field is changed (Fig. 7). Multiple droplets form a supersolid in an elongated trap (Fig. 8), and the supersolidity was corroborated by the excitation of the out-of-phase Goldstone mode (Fig. 9).

A torus-shaped droplet may be generated experimentally by the following procedure. First, the condensate atoms are prepared in the $|F, m = 0\rangle$ hyperfine state in an optical trap. When the DDI is large, this nonmagnetized state is dynamically and energetically unstable against spontaneous magnetization [51]. If the BEC is confined to the expected droplet size, the spontaneous magnetization will form the magnetic-vortex state that has the lowest energy [45]. After some relaxation time, the optical trap is switched off, which results in a self-bound torus-shaped droplet. When hyperfine spins with higher energies ($F \neq 6$) are used, the above experimental procedure must be accomplished within the lifetime due to hyperfine exchanging collisions, which has not been measured for a europium BEC.

Acknowledgment. This work was supported by JSPS KAKENHI Grant No. JP23K03276.

---

[1] For example, see C. Kittel, *Introduction to Solid State Physics*, 8th ed. (Wiley, New Jersey, 2005), Chap. 12.

[2] A. Tonomura, T. Matsuda, J. Endo, T. Arii, and K. Mihama, Direct observation of fine structure of magnetic domain walls by electron holography, Phys. Rev. Lett. **44**, 1430 (1980).

[3] R. P. Cowburn, D. K. Koltsolv, A. O. Adeyeye, M. E. Welland, and D. M. Tricker, Single-domain circular nanomagnets, Phys. Rev. Lett. **83**, 1042 (1999).

[4] T. Shinjo, T. Okuno, R. Hassdorf, K. Shigeto, and T. Ono, Magnetic vortex core observation in circular dots of permalloy, Science **289**, 930 (2000).

[5] J. Rothman, M. Kläui, L. Lopez-Diaz, C. A. F. Vaz, A. Bleloch, J. A. C. Bland, Z. Cui, and R. Speaks, Observation of a bi-domain state and nucleation free switching in mesoscopic ring magnets, Phys. Rev. Lett. **86**, 1098 (2001).

[6] S. P. Li, D. Peyrade, M. Natali, A. Lebib, Y. Chen, U. Ebels, L. D. Buda, and K. Ounadjela, Flux closure structures in cobalt rings, Phys. Rev. Lett. **86**, 1102 (2001).

[7] A. Wachowiak, J. Wiebe, M. Bode, O. Pietzsch, M. Morgenstern, and R. Wiesendanger, Direct observation of internal spin structure of magnetic vortex cores, Science **298**, 577 (2002).

[8] M. J. Hÿtch, R. E. Dunin-Borkowski, M. R. Scheinfein, J. Moulin, C. Duhamel, F. Mazaleyrat, and Y. Champion, Vortex flux channeling in magnetic nanoparticle chains, Phys. Rev. Lett. **91**, 257207 (2003).

[9] C.-J. Jia, L.-D. Sun, F. Luo, X.-D. Han, L. J. Heyderman, Z.-G. Yan, C.-H. Yan, K. Zheng, Z. Zhang, M. Takano, N. Hayashi, M. Eltschka, M. Kläui, U. Rüdiger, T. Kasama, L. Cervera-Gontard, R. E. Dunin-Borkowski, G. Tzvetkov, and J. Raabe, Large-scale synthesis of single-crystalline iron oxide magnetic nanorings, J. Am. Chem. Soc. **130**, 16968 (2008).

[10] G. R. Lewis, J. C. Loudon, R. Tovey, Y.-H. Chen, A. P. Roberts, R. J. Harrison, P. A. Midgley, and E. Ringe, Magnetic vortex states in toroidal iron oxide nanoparticles: Combining micromagnetics with tomography, Nano Lett. **20**, 7405 (2020).

[11] R. P. Cowburn, Magnetic nanodots for device applications, J. Magn. Magn. Mater. **242-245**, 505 (2002).

[12] D.-H. Kim, E. A. Rozhkova, I. V. Ulasov, S. D. Bader, T. Rajh, M. S. Lesniak, and V. Novosad, Biofunctionalized magnetic-vortex microdiscs for targeted cancer-cell destruction, Nat. Mater. **9**, 165 (2010).

[13] J. Torrejon, M. Riou, F. A. Araujo, S. Tsunegi, G. Khalsa, D. Querlioz, P. Bortolotti, V. Cros, K. Yakushiji, A. Fukushima, H. Kubota, S. Yuasa, M. D. Stiles, and J. Grollier, Neuromorphic computing with nanoscale spintronic oscillators, Nature (London) **547**, 428 (2017).

[14] X. Liu, N. Kent, A. Ceballos, R. Streubel, Y. Jiang, Y. Chai, P. Y. Kim, J. Forth, F. Hellman, S. Shi, D. Wang, B. A. Helms, P. D. Ashby, P. Fischer, and T. P. Russell, Reconfigurable ferromagnetic liquid droplets, Science **365**, 264 (2019).

[15] D. S. Petrov, Quantum mechanical stabilization of a collapsing Bose-Bose mixture, Phys. Rev. Lett. **115**, 155302 (2015).

[16] T. D. Lee, K. Huang, and C. N. Yang, Eigenvalues and eigenfunctions of a Bose system of hard spheres and its low-temperature properties, Phys. Rev. **106**, 1135 (1957).

[17] H. Kadau, M. Schmitt, M. Wenzel, C. Wink, T. Maier, I. Ferrier-Barbut, and T. Pfau, Observing the Rosensweig instability of a quantum ferrofluid, Nature (London) **530**, 194 (2016).

[18] M. Schmitt, M. Wenzel, F. Böttcher, I. Ferrier-Barbut, and T. Pfau, Self-bound droplets of a dilute magnetic quantum liquid, Nature (London) **539**, 259 (2016).

[19] I. Ferrier-Barbut, H. Kadau, M. Schmitt, M. Wenzel, and T. Pfau, Observation of quantum droplets in a strongly dipolar Bose gas, Phys. Rev. Lett. **116**, 215301 (2016).

[20] L. Chomaz, S. Baier, D. Petter, M. J. Mark, F. Wächtler, L. Santos, and F. Ferlaino, Quantum-fluctuation-driven crossover from a dilute Bose-Einstein condensate to a macrodroplet in a dipolar quantum fluid, Phys. Rev. X **6**, 041039 (2016).

[21] I. Ferrier-Barbut, M. Wenzel, F. Böttcher, T. Langen, M. Isoard, S. Stringari, and T. Pfau, Scissors mode of dipolar quantum droplets of dysprosium atoms, Phys. Rev. Lett. **120**, 160402 (2018).

[22] C. R. Cabrera, L. Tanzi, J. Sanz, B. Naylor, P. Thomas, P. Cheiney, and L. Tarruell, Quantum liquid droplets in a mixture of Bose-Einstein condensates, Science **359**, 301 (2018).

[23] G. Semeghini, G. Ferioli, L. Masi, C. Mazzinghi, L. Wolswijk, F. Minardi, M. Modugno, G. Modugno, M. Inguscio, and M. Fattori, Self-bound quantum droplets of atomic mixtures in free space, Phys. Rev. Lett. **120**, 235301 (2018).

[24] P. Cheiney, C. R. Cabrera, J. Sanz, B. Naylor, L. Tanzi, and L. Tarruell, Bright soliton to quantum droplet transition in a mixture of Bose-Einstein condensates, Phys. Rev. Lett. **120**, 135301 (2018).

[25] F. Wächtler and L. Santos, Quantum filaments in dipolar Bose-Einstein condensates, Phys. Rev. A **93**, 061603 (R) (2016).

[26] F. Wächtler and L. Santos, Ground-state properties and elementary excitations of quantum droplets in dipolar Bose-Einstein condensates, Phys. Rev. A **94**, 043618 (2016).

[27] H. Saito, Path-integral Monte Carlo study on a droplet of a dipolar Bose-Einstein condensate stabilized by quantum fluctuation, J. Phys. Soc. Jpn. **85**, 053001 (2016).

[28] R. N. Bisset, R. M. Wilson, D. Baillie, and P. B. Blakie, Ground-state phase diagram of a dipolar condensate with quantum fluctuations, Phys. Rev. A **94**, 033619 (2016).

[29] A. Macia, J. Sánchez-Baena, J. Boronat, and F. Mazzanti, Droplets of trapped quantum dipolar bosons, Phys. Rev. Lett. **117**, 205301 (2016).

[30] D. Baillie, R. M. Wilson, and P. B. Blakie, Collective excitations of self-bound droplets of a dipolar quantum fluid, Phys. Rev. Lett. **119**, 255302 (2017).

[31] M. Wenzel, F. Böttcher, T. Langen, I. Ferrier-Barbut, and T. Pfau, Striped states in a many-body system of tilted dipoles, Phys. Rev. A **96**, 053630 (2017).

[32] A. Cidrim, F. E. A. dos Santos, E. A. L. Henn, and T. Macrí, Vortices in self-bound dipolar droplets, Phys. Rev. A **98**, 023618 (2018).

[33] F. Böttcher, M. Wenzel, J.-N. Schmidt, M. Guo, T. Langen, I. Ferrier-Barbut, T. Pfau, R. Bombín, J. Sánchez-Baena, J. Boronat, and F. Mazzanti, Dilute dipolar quantum droplets beyond the extended Gross-Pitaevskii equation, Phys. Rev. Res. **1**, 033088 (2019).

[34] R. Ołdziejewski, W. Górecki, K. Pawłowski, and K. Rzążewski, Strongly correlated quantum droplets in quasi-1D dipolar Bose gas, Phys. Rev. Lett. **124**, 090401 (2020).

[35] R. N. Bisset, L. A. Peña Ardila, and L. Santos, Quantum droplets of dipolar mixtures, Phys. Rev. Lett. **126**, 025301 (2021).

[36] J. C. Smith, D. Baillie, and P. B. Blakie, Quantum droplet states of a binary magnetic gas, Phys. Rev. Lett. **126**, 025302 (2021).

[37] A.-C. Lee, D. Baillie, and P. B. Blakie, Numerical calculation of dipolar-quantum-droplet stationary states, Phys. Rev. Res. **3**, 013283 (2021).

[38] M. Boninsegni, Morphology of dipolar Bose droplets, Results Phys. **31**, 104935 (2021).

[39] J. Kopyciński, M. Łebek, W. Górecki, and K. Pawłowski, Ultrawide dark solitons and droplet-soliton coexistence in a dipolar Bose gas with strong contact interactions, Phys. Rev. Lett. **130**, 043401 (2023).

[40] S. Yi, L. You, and H. Pu, Quantum phases of dipolar spinor condensates, Phys. Rev. Lett. **93**, 040403 (2004).

[41] Y. Kawaguchi, H. Saito, and M. Ueda, Einstein–de Haas effect in dipolar Bose-Einstein condensates, Phys. Rev. Lett. **96**, 080405 (2006).

[42] L. Santos and T. Pfau, Spin-3 chromium Bose-Einstein condensates, Phys. Rev. Lett. **96**, 190404 (2006).

[43] R. B. Diener and T.-L. Ho, ^{52}Cr spinor condensate: A biaxial or uniaxial spin nematic, Phys. Rev. Lett. **96**, 190405 (2006).

[44] S. Yi and H. Pu, Spontaneous spin textures in dipolar spinor condensates, Phys. Rev. Lett. **97**, 020401 (2006).

[45] Y. Kawaguchi, H. Saito, and M. Ueda, Spontaneous circulation in ground-state spinor dipolar Bose-Einstein condensates, Phys. Rev. Lett. **97**, 130404 (2006).

[46] Y. Kawaguchi, H. Saito, and M. Ueda, Can spinor dipolar effects be observed in Bose-Einstein condensates? Phys. Rev. Lett. **98**, 110406 (2007).

[47] M. Takahashi, S. Ghosh, T. Mizushima, and K. Machida, Spinor dipolar Bose-Einstein condensates: Classical spin approach, Phys. Rev. Lett. **98**, 260403 (2007).

[48] K. Gawryluk, M. Brewczyk, K. Bongs, and M. Gajda, Resonant Einstein–de Haas effect in a rubidium condensate, Phys. Rev. Lett. **99**, 130401 (2007).

[49] B. Sun and L. You, Observing the Einstein–de Haas effect with atoms in an optical lattice, Phys. Rev. Lett. **99**, 150402 (2007).

[50] M. Yasunaga and M. Tsubota, Spin echo in spinor dipolar Bose-Einstein condensates, Phys. Rev. Lett. **101**, 220401 (2008).

[51] S. Hoshi and H. Saito, Symmetry-breaking magnetization dynamics of spinor dipolar Bose-Einstein condensates, Phys. Rev. A **81**, 013627 (2010).

[52] T. Świsłocki, M. Brewczyk, M. Gajda, and K. Rzążewski, Spinor condensate of ^{87}Rb as a dipolar gas, Phys. Rev. A **81**, 033604 (2010).

[53] J. A. M. Huhtamäki, M. Takahashi, T. P. Simula, T. Mizushima, and K. Machida, Spin textures in condensates with large dipole moments, Phys. Rev. A **81**, 063623 (2010).

[54] F. Deuretzbacher, G. Gebreyesus, O. Topic, M. Scherer, B. Lücke, W. Ertmer, J. Arlt, C. Klempt, and L. Santos, Parametric amplification of matter waves in dipolar spinor Bose-Einstein condensates, Phys. Rev. A **82**, 053608 (2010).

[55] K. Kudo and Y. Kawaguchi, Hydrodynamic equation of a spinor dipolar Bose-Einstein condensate, Phys. Rev. A **82**, 053614 (2010).

[56] T. P. Simula, J. A. M. Huhtamäki, M. Takahashi, T. Mizushima, and K. Machida, Rotating dipolar spin-1 Bose-Einstein condensates, J. Phys. Soc. Jpn. **80**, 013001 (2011).

[57] K. Gawryluk, K. Bongs, and M. Brewczyk, How to observe dipolar effects in spinor Bose-Einstein condensates, Phys. Rev. Lett. **106**, 140403 (2011).

[58] B. Pasquiou, E. Maréchal, G. Bismut, P. Pedri, L. Vernac, O. Gorceix, and B. Laburthe-Tolra, Spontaneous demagnetization of a dipolar spinor Bose gas in an ultralow magnetic field, Phys. Rev. Lett. **106**, 255303 (2011).

[59] Y. Eto, H. Saito, and T. Hirano, Observation of dipole-induced spin texture in an ^{87}Rb Bose-Einstein condensate, Phys. Rev. Lett. **112**, 185301 (2014).

[60] G. E. Marti, A. MacRae, R. Olf, S. Lourette, F. Fang, and D. M. Stamper-Kurn, Coherent magnon optics in a ferromagnetic spinor Bose-Einstein condensate, Phys. Rev. Lett. **113**, 155302 (2014).

[61] H. Saito and M. Kunimi, Energy shift of magnons in a ferromagnetic spinor-dipolar Bose-Einstein condensate, Phys. Rev. A **91**, 041603(R) (2015).

[62] T. Oshima and Y. Kawaguchi, Spin Hall effect in a spinor dipolar Bose-Einstein condensate, Phys. Rev. A **93**, 053605 (2016).

[63] M. O. Borgh, J. Lovegrove, and J. Ruostekoski, Internal structure and stability of vortices in a dipolar spinor Bose-Einstein condensate, Phys. Rev. A **95**, 053601 (2017).

[64] B. Liao, S. Li, C. Huang, Z. Luo, W. Pang, H. Tan, B. A. Malomed, and Y. Li, Anisotropic semivortices in dipolar spinor condensates controlled by Zeeman splitting, Phys. Rev. A **96**, 043613 (2017).

[65] S. Lepoutre, K. Kechadi, B. Naylor, B. Zhu, L. Gabardos, L. Isaev, P. Pedri, A. M. Rey, L. Vernac, and B. Laburthe-Tolra, Spin mixing and protection of ferromagnetism in a spinor dipolar condensate, Phys. Rev. A **97**, 023610 (2018).

[66] Y. Miyazawa, R. Inoue, H. Matsui, G. Nomura, and M. Kozuma, Bose-Einstein condensation of europium, Phys. Rev. Lett. **129**, 223401 (2022).

[67] D. J. Papoular, G. V. Shlyapnikov, and J. Dalibard, Microwave-induced Fano-Feshbach resonances, Phys. Rev. A **81**, 041603(R) (2010).

[68] L. D. Landau and E. M. Lifshitz, *Quantum Mechanics*, 3rd ed. (Butterworth-Heinemann, Oxford, 1981), Sec. 121.

[69] A. A. Buchachenko, G. Chałasiński, and M. M. Szczęśniak, Europium dimer: van der Waals molecule with extremely weak antiferromagnetic spin coupling, J. Chem. Phys. **131**, 241102 (2009).

[70] Y. V. Suleimanov, Zeeman relaxation of magnetically trapped Eu atoms, Phys. Rev. A **81**, 022701 (2010).

[71] S. Uchino, M. Kobayashi, and M. Ueda, Bogoliubov theory and Lee-Huang-Yang corrections in spin-1 and spin-2 Bose-Einstein condensates in the presence of the quadratic Zeeman effect, Phys. Rev. A **81**, 063632 (2010).

[72] T. A. Yoğurt, A. Keleş, and M. Ö. Oktel, Spinor boson droplets stabilized by spin fluctuations, Phys. Rev. A **105**, 043309 (2022).

[73] R. Schützhold, M. Uhlmann, Y. Xu, and U. R. Fischer, Mean-field expansion in Bose-Einstein condensates with finite-range interactions, Intl. J. Mod. Phys. B **20**, 3555 (2006).

[74] A. R. P. Lima and A. Pelster, Quantum fluctuations in dipolar Bose gases, Phys. Rev. A **84**, 041604(R) (2011).

[75] A. R. P. Lima and A. Pelster, Beyond mean-field low-lying excitations of dipolar Bose gases, Phys. Rev. A **86**, 063609 (2012).

[76] See Supplemental Material at http://link.aps.org/supplemental/10.1103/PhysRevResearch.6.L042049 for movies showing the dynamics of the system.

[77] W.-G. Jin, T. Endo, T. Wakui, H. Uematsu, T. Minowa, and H. Katsuragawa, Measurements of the hyperfine structure and $\Delta F = +2$ transitions in Eu I by high-resolution Diode-Laser spectroscopy, J. Phys. Soc. Jpn. **71**, 1905 (2002).

[78] O. W. Richardson, A mechanical effect accompanying magnetization, Phys. Rev. Ser. I **26**, 248 (1908).

[79] A. Einstein and W. J. de Haas, Experimental proof of Ampére's molecular currents, Verh. Dtsch. Phys. Ges. **17**, 152 (1915).

[80] L. Tanzi, E. Lucioni, F. Famá, J. Catani, A. Fioretti, C. Gabbanini, R. N. Bisset, L. Santos, and G. Modugno, Observation of a dipolar quantum gas with metastable supersolid properties, Phys. Rev. Lett. **122**, 130405 (2019).

[81] F. Böttcher, J.-N. Schmidt, M. Wenzel, J. Hertkorn, M. Guo, T. Langen, and T. Pfau, Transient supersolid properties in an array of dipolar quantum droplets, Phys. Rev. X **9**, 011051 (2019).

[82] L. Chomaz, D. Petter, P. Ilzhöfer, G. Natale, A. Trautmann, C. Politi, G. Durastante, R. M. W. van Bijnen, A. Patscheider, M. Sohmen, M. J. Mark, and F. Ferlaino, Long-lived and transient supersolid behaviors in dipolar quantum gases, Phys. Rev. X **9**, 021012 (2019).

[83] T.-L. Ho, Spinor Bose condensates in optical traps, Phys. Rev. Lett. **81**, 742 (1998).

[84] M. Guo, F. Böttcher, J. Hertkorn, J.-N. Schmidt, M. Wenzel, H. P. Büchler, T. Langen, and T. Pfau, The low-energy Goldstone mode in a trapped dipolar supersolid, Nature (London) **574**, 386 (2019).